Modeling and Increasing the High-Frequency Impedance of Single-Layer Mn-Zn Ferrite Toroidal Inductors With Electromagnetic Analysis

Yiming Li, *Student Member, IEEE*, and Shuo Wang, *Fellow, IEEE*

***Abstract*—This article first investigates the equivalent parallel capacitance (EPC) and equivalent parallel resistance (EPR) due to the electromagnetic field inside the Mn-Zn ferrite toroidal cores of the inductors with a single-layer winding based on electromagnetic theory. From the investigation, the effects of core's cross-sectional shape and number of winding turns on the EPC and EPR are explored. A stacked core structure was studied to increase the inductor's high-frequency (HF) impedance for electromagnetic interference suppression. The article further investigated the EPC due to the electric field energy in the space between winding turns, and between the winding turns and the core. The effect of the number of winding turns on total EPC was also explored. The technique to achieve high HF impedance was proposed with an optimal number of winding turns. Both simulations and experiments were conducted to validate the developed theory and techniques.**

***Index Terms*—Electromagnetic (EM) field, equivalent parallel capacitance (EPC), equivalent parallel resistance (EPR), inductor, Mn-Zn ferrite.**

I. Introduction

INDUCTANCE is an important parameter of a conventional magnetic inductor to achieve an inductor's basic functionality, however, the inductor's high-frequency (HF) impedance, which is mostly determined by the parasitics, including the equivalent parallel capacitance (EPC) and the equivalent parallel resistance (EPR), is very important for the applications of HF electromagnetic interference (EMI) noise suppression [13]. To reduce EMI noise spikes at HFs, the inductor should have high impedance at these frequencies. Fig. 1 shows a wire-wounded toroidal inductor and its conventional first-order equivalent circuit model including both EPC and EPR.

In Fig. 1(b), L is the inductance of the inductor in Fig. 1(a). EPR represents the power loss (P) dissipated within the magnetic core if the winding power loss is ignored. The analytical approaches were proposed in [1] and [2] to calculate P and its corresponding EPR. EPC represents the total electric field energy (E_E) of the inductor. The electric field energy of an inductor exists inside both the core and the space. Many existing studies in the literature assumed that most of the electric field energy is in the space. The most distinguished and highly cited works are [3] and [4]. In [3] and [4], the parasitic capacitances of an inductor were classified as three parts—the parasitic capacitance between two winding turns, between winding turns and the magnetic core, and between winding layers. Each part was calculated based on electrostatic analysis. Other studies [5], [6] focused on the electric field energy inside the magnetic core. The energy was calculated from the induced vortex electric field due to the time-varying magnetic field inside the magnetic core. Within commonly used ferrite materials, Mn-Zn ferrite has high permittivity (ε_r: 10^5–10^6), so the electric field energy inside the magnetic core is not ignorable. On the other hand, the permittivity of Ni-Zn ferrite is not high (ε_r: 10–100), so the electric field energy inside the magnetic core is not as important as that in Mn-Zn ferrite.

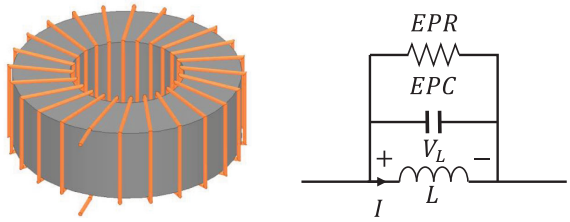

Fig. 1. (a) Wire-wounded toroid inductor. (b) Inductor circuit model.

Recently, some researchers pointed out that both the electric field energy inside the core and in the space may be important [7], [8]. In [8], based on measurement results, it is found that if the number of winding turns is small, the resonant frequencies of the inductors are almost constant even when the number of winding turns changes. It was also found that the EPC due to the electric field energy inside the core is inversely proportional to the square of the number of winding turns. However, [8] did not study the fundamentals behind these findings. Our paper [7] presented and investigated our findings based on a simplified theory for the electric field energy inside the magnetic core, but the fundamental behind it has not been fully explored.

Furthermore, in the studies above, the inductor core and winding design techniques to reduce the parasitics based on the

Manuscript received January 5, 2020; revised March 28, 2020; accepted June 10, 2020. Date of publication November 23, 2020; date of current version February 5, 2021. This work was supported by the National Science Foundation under Award 1611048. Recommended for publication by Associate Editor F. Luo. *(Corresponding author: Shuo Wang.)*

The authors are with the Department of Electrical and Computer Engineering, University of Florida, Gainesville, FL 32608 USA (e-mail: brighturan@ufl.edu; shuowang@ieee.org).

Color versions of one or more of the figures in this article are available at https://doi.org/10.1109//TPEL.2020.3039809.

Digital Object Identifier 10.1109/TPEL.2020.3039809

electromagnetics were not explored. The objective of this article is to investigate and model EPC and EPR of magnetic inductors and to develop inductor design techniques to achieve high HF impedance. For the model in Fig. 1(b), at frequencies higher than $\frac{1}{2\pi\sqrt{\mathrm{EPC}\times\mathrm{L}}}$ or $\frac{\mathrm{EPR}}{2\pi L}$ when the impedance of L can be ignored, the admittance Y_L of the inductor is

$$Y_L = \frac{1}{EPR} + sEPC + \frac{1}{sL} \approx \frac{1}{EPR} + sEPC. \tag{1}$$

In (1), the magnitude of Y_L is the minimum when EPR reaches the maximum and EPC reaches the minimum. Since the EPC and EPR represent E_E and P within an inductor, respectively, they can be expressed as

$$EPC = \frac{4E_E}{|V_L|^2} \tag{2}$$

$$EPR = \frac{|V_L|^2}{2P} \tag{3}$$

where $|V_L|$ is the amplitude of the voltage across the inductor. Based on (1)–(3), both E_E and P should be minimized to increase the inductor's HF impedance.

From electromagnetics point of view, if conductivity is σ, permeability $\mu = \mu' - \mathrm{j}\mu''$, permittivity $\varepsilon = \varepsilon' - \mathrm{j}\varepsilon''$, where ε_0 and μ_0 are the permittivity and permeability of the air, the magnetic field energy E_H, electric field energy E_E, and power loss P within an inductor in Fig. 1(b) are given in (4)–(6), respectively

$$E_H = \frac{L}{4}|I|^2 \approx \int_{V_{Core}} \frac{\mu'}{4}|H|^2 dv \tag{4}$$

$$E_E = \frac{EPC}{4}|V_L|^2 = \int_{V_{Space}} \frac{\varepsilon_0}{4}|E|^2 dv + \int_{V_{Core}} \frac{\varepsilon'}{4}|E|^2 dv \tag{5}$$

$$\begin{aligned} P &= \frac{|V_L|^2}{2EPR} = P_E + P_H + P_D \\ &= \int_{V_{Core}} \frac{1}{2}\sigma|E|^2 dv + \int_{V_{Core}} \frac{1}{2}\omega\mu''|H|^2 dv \\ &\quad + \int_{V_{Core}} \frac{1}{2}\omega\varepsilon''|E|^2 dv \end{aligned} \tag{6}$$

where I, H, and E are the current flowing through the inductance, the magnetic field intensity, and the electric field intensity (all of them are in amplitude), respectively. The power loss P is composed of eddy current power loss P_E, hysteresis power loss P_H, and dielectric power loss P_D [2].

In (4), since a ferrite core's μ' is much higher than that of the air, E_H is assumed to be concentrated in the magnetic core. On the other hand, for the electric field energy, both the energy in the space and in the core should be considered.

The rest of this article is organized as follows. In Section II, the analytical approaches are introduced to derive the electric field energy, magnetic field energy, and power loss inside the magnetic core. Since the analytical solution is very complicated, some important principles will be derived from the analytical solution for inductor optimal design. The effects of the number of winding turns and the core's cross-sectional shape on EPC and EPR will be discussed. Stacked core structures will be investigated to increase the inductor's HF impedance. In Section III, the electric field energy in the space will be analyzed. The EPC associated with the electric field energy in the space is derived for a single-layer toroidal inductor. The design of the number of winding turns is investigated to increase the inductor's HF impedance. In Section IV, experiments are conducted to verify the developed theory and techniques. In Section V, a parametric study and a discussion are presented. Finally, Section VI concludes this article.

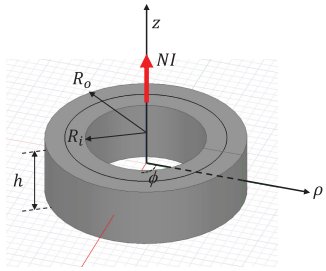

Fig. 2. Geometry of a toroidal magnetic core.

II. Energy Inside a Magnetic Core and Techniques to Reduce EPC and Increase EPR

A. Electric Field Energy Inside a Magnetic Core

Fig. 2 shows the geometry of a toroidal magnetic core in the cylindrical coordinate, where R_o and R_i represent the outer and inner radius and h represents the height of the core. It is assumed that for the EMI noise, the magnetic material is homogeneous, isotropic, and linear. Since the permeability of the core is much larger than that of the air, the magnetic flux outside the core can be ignored for E_H calculation. Due to the circular symmetry, the magnetic flux inside the core only exists in ϕ-direction. As a result, the induced electric field inside the core only has ρ and z components. The magnetic field inside the core satisfies the following [5]:

$$\frac{\partial^2 H_\phi}{\partial\rho^2} + \frac{1}{\rho}\frac{\partial H_\phi}{\partial\rho} - \frac{H_\phi}{\rho^2} + \frac{\partial^2 H_\phi}{\partial z^2} - \gamma^2 H_\phi = \gamma^2 H_{\phi 0} \tag{7}$$

where the magnetic field is decomposed to the incident magnetic field ($H_{\phi 0}$) plus the induced magnetic field (H_ϕ).

If the number of winding turns is N, $H_{\phi 0}$ and γ^2 are

$$H_{\phi 0} = \frac{NI}{2\pi\rho} \tag{8}$$

$$\gamma^2 = j\omega\mu(\sigma + j\omega\varepsilon). \tag{9}$$

The boundary conditions for the induced H_ϕ are

$$H_\phi|_{z=\pm\frac{h}{2}} = 0,\ R_i < \rho < R_o \tag{10}$$

$$H_\phi|_{\rho=R_i,\ R_o} = 0, -\frac{h}{2} < z < \frac{h}{2}. \tag{11}$$

The solution of H_ϕ is then given by (12), and the associated electric field along ρ and z directions are given by (13) and (14)

in the following:

$$H_\phi = \sum_{s=1}^{\infty}\sum_{n=0}^{\infty} A_{sn} \times \cos\frac{(2n+1)\,\pi z}{h}\left\{\frac{J_1(\alpha_s\rho)}{J_1(\alpha_s R_i)} - \frac{Y_1(\alpha_s\rho)}{Y_1(\alpha_s R_i)}\right\} \quad (12)$$

$$E_\rho = -\frac{1}{\sigma+j\omega\varepsilon}\frac{\partial H_\phi}{\partial z} = \frac{1}{\sigma+j\omega\varepsilon} \times \sum_{s=1}^{\infty}\sum_{n=0}^{\infty} A_{sn}\frac{(2n+1)\,\pi}{h} \times \sin\frac{(2n+1)\,\pi z}{h} \times\left\{\frac{J_1(\alpha_s\rho)}{J_1(\alpha_s R_i)} - \frac{Y_1(\alpha_s\rho)}{Y_1(\alpha_s R_i)}\right\} \quad (13)$$

$$E_z = \frac{1}{\sigma+j\omega\varepsilon}\left(\frac{\partial H_\phi}{\partial\rho} + \frac{H_\phi}{\rho}\right) = \frac{1}{\sigma+j\omega\varepsilon} \times \sum_{s=1}^{\infty}\sum_{n=0}^{\infty}\alpha_s A_{sn} \times \cos\frac{(2n+1)\,\pi z}{h} \times\left\{\frac{J_0(\alpha_s\rho)}{J_1(\alpha_s R_i)} - \frac{Y_0(\alpha_s\rho)}{Y_1(\alpha_s R_i)}\right\} \quad (14)$$

where A_{sn} is given by the following and $\alpha_s R_i$ is the sth zero of the cross product of $J_1(\alpha_s R_i)Y_1(\alpha_s R_o) - J_1(\alpha_s R_o)Y_1(\alpha_s R_i) = 0$:

$$A_{sn} = -\frac{2\gamma^2 NI}{\pi}\frac{(-1)^n}{2n+1}\frac{J_1(\alpha_s R_i)\,J_1(\alpha_s R_o)\,Y_1(\alpha_s R_i)}{[(2n+1)\,\pi/h]^2 + \alpha_s^2 + \gamma^2} \times \frac{R_i J_1(\alpha_s R_i) - R_o J_1(\alpha_s R_o)}{R_i R_o\,[J_1^2(\alpha_s R_i) - J_1^2(\alpha_s R_o)]}. \quad (15)$$

Therefore, the magnetic field energy E_{HCore}, the electric field energy E_{ECore}, and the power loss P inside the core are

$$E_{HCore} = \frac{1}{4}\,\mu' \int_{-\frac{1}{2}h}^{\frac{1}{2}h}\int_{R_i}^{R_o} |H_\phi + H_{\phi 0}|^2 2\pi\rho d\rho dz \quad (16)$$

$$E_{ECore} = \frac{1}{4}\,\varepsilon' \int_{-\frac{1}{2}h}^{\frac{1}{2}h}\int_{R_i}^{R_o} \left(|E_\rho|^2 + |E_z|^2\right) 2\pi\rho d\rho dz \quad (17)$$

$$\begin{aligned} P &= \frac{1}{2}\,\sigma \int_{-\frac{1}{2}h}^{\frac{1}{2}h}\int_{R_i}^{R_o} \left(|E_\rho|^2 + |E_z|^2\right) 2\pi\rho d\rho dz \\ &\quad + \frac{1}{2}\omega\mu'' \int_{-\frac{1}{2}h}^{\frac{1}{2}h}\int_{R_i}^{R_o} |H_\phi + H_{\phi 0}|^2 2\pi\rho d\rho dz \\ &\quad + \frac{1}{2}\omega\varepsilon'' \int_{-\frac{1}{2}h}^{\frac{1}{2}h}\int_{R_i}^{R_o} \left(|E_\rho|^2 + |E_z|^2\right) 2\pi\rho d\rho dz \\ &\approx \frac{1}{2}\sigma \int_{-\frac{1}{2}h}^{\frac{1}{2}h}\int_{R_i}^{R_o} \left(|E_\rho|^2 + |E_z|^2\right) 2\pi\rho d\rho dz = P_E. \end{aligned} \quad (18)$$

For the Mn-Zn ferrite used in EMI suppression, conductivity σ is usually high so it can dissipate EMI noise with high eddy current power loss. For example, the J material from Magnetics Inc. has $\sigma = 2$ S/m. On the other hand, P_H and P_D only contribute to a small part of the power loss [16]. So, the eddy current power loss P_E dominates total power loss P at HFs in (18).

If the cross-sectional area of the core is A_e, the voltage V_L across the inductor is

$$V_L = -j\omega N \oint \vec{B}\cdot d\overrightarrow{A_e} = -j\omega N\mu \oint (H_\phi + H_{\phi 0})\,dA_e. \quad (19)$$

Based on the model in Fig. 1, a parallel resonance happens when the impedance of L cancels that of EPC. If EPC is only contributed by the electric field energy inside the core, the resonance frequency $f_{r\mathrm{core}}$ can be expressed by the following, where $\mathrm{EPC_{core}}$ is the EPC due to the electric field energy inside the core:

$$f_{rcore} = \frac{1}{2\pi\sqrt{L \times EPC_{core}}}. \quad (20)$$

From the electromagnetics point of view, the resonance happens at $\omega_{rcore} = 2\pi f_{rcore}$ that meets the condition in the following:

$$E_{ECore}\ (\omega_{rcore}) = E_{HCore}\ (\omega_{rcore}). \quad (21)$$

If $E_{ECore} > E_{HCore}$, the inductor impedance is capacitive; and if $E_{ECore} < E_{HCore}$, the inductor impedance is inductive. At frequencies $\omega = 2\pi f > \omega_{rcore}$, the magnitude of admittance $|Y_L|$ can be expressed as follows, based on (1)–(3) and (17)–(19):

$$|Y_L| = \sqrt{\left|\frac{1}{EPR}\right|^2 + |sEPC|^2} = \frac{\sqrt{(2P)^2 + (4\omega E_{ECore})^2}}{|V_L|^2}. \quad (22)$$

B. Effect of the Number of Winding Turns

When the geometry of the core is fixed, and the frequency f and I are given, based on (2)–(22), magnetic field and electric field H_ϕ, $H_{\phi 0}$, E_ρ, and E_z are proportional to N; the power and energy P_E, P_H, P_D, P, E_{ECore}, and E_{HCore} are proportional to N^2; V_L is proportional to N^2; L and EPR are proportional to N^2; $\mathrm{EPC_{core}}$ and $|Y_L|$ are proportional to $1/N^2$; f_{rcore} or ω_{rcore} will not be influenced by N. It should be noted that if V_L instead of I is given, the conclusions for L, EPR, $\mathrm{EPC_{core}}$, $|Y_L|$, and f_{rcore} are the same.

Because of this, for a magnetic core with fixed geometry, if EPC is dominated by the electric field energy inside the core, increasing N will increase EPR, reduce EPC, and increase HF impedance $1/|Y_L|$.

C. Effect of Cross-Sectional Shape on E_{ECore} and P_E

Based on (13), (14), (17), and (18), the distribution of the electric field inside the core is a function of core dimensions R_i, R_o, and h, so $E_{E\mathrm{Core}}$, P, $\mathrm{EPC_{core}}$, EPR, and inductor's HF impedance will be impacted by the core's crosssectional shape.

In order to investigate the optimal ratio of width to height, the mean magnetic path length (MPL), which is given by (23) as follows, and A_e, which is given by (24) as follows, will be kept constant so that L is almost constant with a given N:

$$MPL = \pi(R_i + R_o) \quad (23)$$

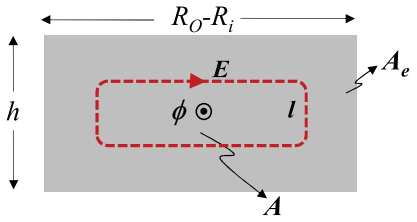

Fig. 3. Induced electric flux on the cross section of the core.

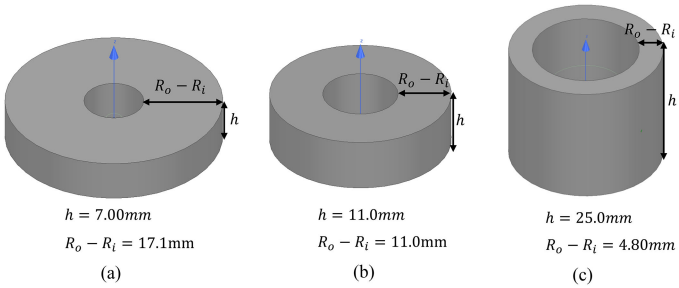

Fig. 4. Different magnetic cores with constant MPL and A_e in Ansys HFSS.

$$A_e = h\,(R_o - R_i)\,. \tag{24}$$

Because A_e and L are constant when the ratio $(R_O{-}R_i)/h$ changes, the total magnetic flux is constant. In Fig. 3, ϕ is the magnetic flux flowing through area A of a rectangular loop $\boldsymbol{l}$ along which an induced electric flux line E approximately flows. A shares the center with A_e.

The induced electric field $\boldsymbol{E}$ meets the following condition:

$$\oint \vec{E}\cdot d\,\vec{l} = -\frac{d\vec{\phi}}{dt}. \tag{25}$$

In (25), when $(R_O{-}R_i)/h$ and the width-to-length ratio of loop $\boldsymbol{l}$ change proportionally, area A does not change, so the ϕ enclosed by $\boldsymbol{l}$ approximately does not change. At the same time, because the square shape gives the shortest $|\boldsymbol{l}|$ for the induced electric flux in the core, based on (25), $|\boldsymbol{E}|$ reaches the maximum when the cross section is a square shape. Because of this, the core with a square cross-sectional shape has the largest E_ρ, E_z, $E_{E\mathrm{core}}$, $\mathrm{EPC}_{\mathrm{core}}$, and the smallest EPR and $f_{r\mathrm{core}}$, and therefore, the smallest HF impedance. A similar conclusion can be drawn for the magnetic core with a round cross-sectional shape.

To verify the analysis above, an inductor is modeled in Ansys HFSS in Fig. 4(a)–(c). The core height h changes from 7 to 25 mm, meanwhile, MPL (MPL = 83 mm) and A_e (A_e = 120 mm^2) remain constant, $\mu_r = 1000$, $\varepsilon_r = 2\times10^5$, and σ = 2 S/m.

To reduce the influence of the electric field energy in the space between winding turns, and between the winding turns and the core on the simulated results, only one turn winding is used in Fig. 4. A current excitation (I = 1 A) is applied along +z-direction (center line).

The simulated inductance L and electric field energy E_{ECore} at 1 MHz are plotted in Fig. 5(a) as a function of h. In Fig. 5(a), as h increases, the inductance is almost constant and the electric field energy reaches the maximum when the cross section is a square. In other words, the impedance of the inductor using the core in Fig. 4(b) tends to become capacitive at lower frequencies than the impedances of those using the cores in Fig. 4(a) and (c). This verified the analysis above.

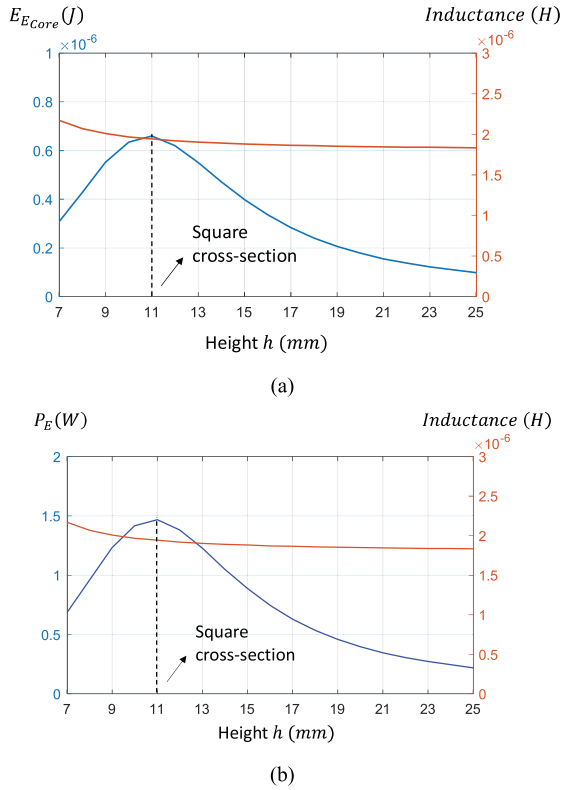

Fig. 5. (a) L and E_{ECore} inside the core at 1 MHz as a function of h. (b) P_E inside the core at 1 MHz as a function of h.

Similarly, based on (18), because $|\boldsymbol{E}|$ reaches the maximum when the cross section is a square shape, the core power loss is the highest, which leads to the smallest EPR, as shown in Fig. 5(b). Based on the analysis above, to have high HF impedance (small EPC and big EPR), the following conditions should be met: $h > (R_o{-}R_i)$ or $h < (R_o{-}R_i)$. However, large h and R_o may lead to high profile, large footprint, and nonoptimized window area, so it may not be always desired. Other technique needs to be explored to solve this issue.

The resonant frequencies $f_{r\mathrm{core}}$ of the inductor as a function of h are further simulated in Ansys and are plotted in Fig. 6. In Fig. 6, $f_{r\mathrm{core}}$ reaches the minimum when the cross-sectional area is a square. This further verified the analysis.

D. Proposed Stacked Magnetic Cores

Since a large or small width-to-height ratio helps reduce EPC and increase EPR but may lead to undesired negative results, stacked core structures are proposed in Fig. 7(b)–(e) to solve the issue. It should be noted that the analytical solutions of the electric field and energy can still be derived based on (7)–(9) and the modified boundary conditions, but finite-element analysis (FEA) simulation is conducted in Ansys HFSS to illustrate the technique in Fig. 7.

Fig. 7(a) shows the normal and Fig. 7(b)–(e) shows the proposed stacked core structures of which each has the combined

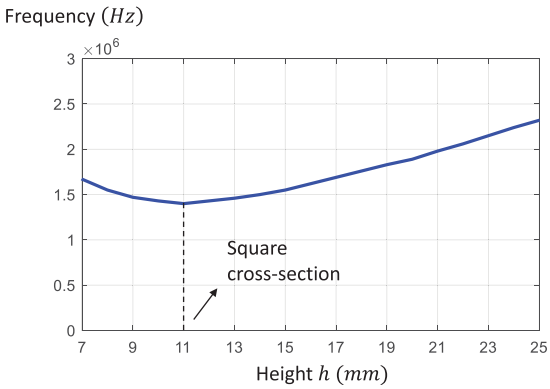

Fig. 6. Resonant frequency of the magnetic cores with various heights.

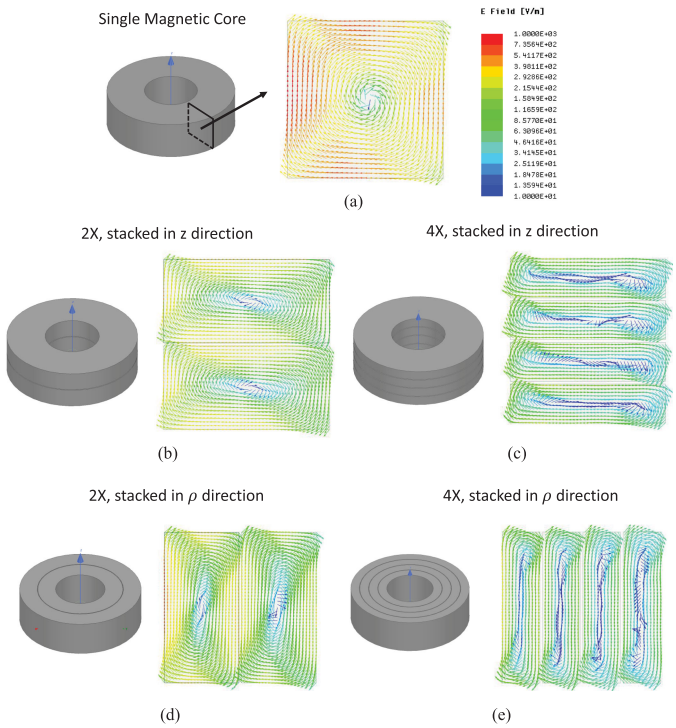

Fig. 7. Simulated electric field: (a) original core, (b) and (c) two and four cores with large width-to-height ratios stacked in z-direction, and (d) and (e) two and four cores with small width-to-height ratios stacked in ρ-direction.

cross-sectional geometry and area same as that in Fig. 4(b). Fig. 7(b) and (c) shows two and four cores, respectively, stacked with large width-to-height ratios in z-direction, and Fig. 7(d) and (e) shows two and four cores with small width-to-height ratios stacked in ρ-direction, respectively. There is a very thin layer of low permittivity coating on the cores so the electric flux will be confined within individual cores. The electric field distributions inside the cores excited with 1 A current at 1 MHz along $+z$-direction (center line) are plotted in the figures with the same scale. The proposed stacked cores can greatly reduce the electric field intensity inside the cores.

The total electric field energy $E_{E\mathrm{Core}}$, eddy current power loss P_E, and $f_{r\mathrm{core}}$ inside the cores of the inductors in Fig. 7 are listed in Table I. It is shown that $E_{E\mathrm{Core}}$ and P_E of the stacked cores

TABLE I
ELECTRIC FIELD ENERGY, EDDY CURRENT POWER LOSS, AND RESONANT FREQUENCY OF DIFFERENT CORES

Core Format	E_{ECore} at 1MHz (J)	f_{rcore} (Hz)	P_E at 1MHz (mW)
1×, normal	6.59×10^{-7}	1.40×10^{6}	1470
2×, z direction	1.11×10^{-7}	2.16×10^{6}	252
4×, z direction	2.67×10^{-8}	3.97×10^{6}	60.4
2×, ρ direction	1.08×10^{-7}	2.22×10^{6}	244
4×, ρ direction	2.57×10^{-8}	4.03×10^{6}	58.1

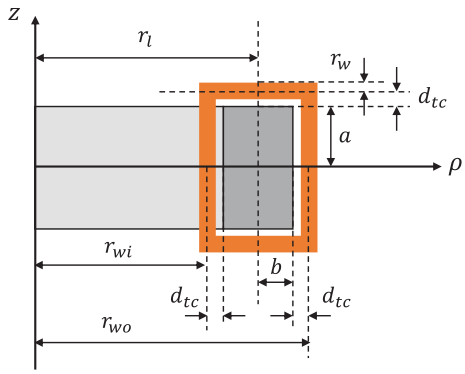

Fig. 8. Cross-sectional view of a toroidal inductor with single winding layer.

are much lower than those of the original core. As a result, the resonant frequency $f_{r\mathrm{core}}$ increases greatly as expected.

III. Electric Field Energy in the Space and Techniques to Improve Inductor Winding Design

A. Turn-to-Core and Turn-to-Turn Capacitance

The electric field energy inside the core was calculated based on time-varying electromagnetic (EM) theory in Section II because the wavelength (0.7 mm @ 30 MHz) of the EM wave is much smaller or comparable to the dimensions of the core in conductive EMI frequency range up to 30 MHz due to the high permeability ($\mu_r = 10^3$) and high permittivity ($\varepsilon_r = 2\times10^5$) of the core. On the other hand, for the electric field in the space, the wavelength (10 m @ 30 MHz) of the EM wave is much larger than the dimension of the inductor due to the low permeability and permittivity of the space, so electrostatic analysis can be used for electric field energy calculation.

An accurate analytical solution of the electric field in the space is a 3-D boundary problem, which is very difficult to solve. Therefore, an approximate model with good accuracy is proposed here to calculate the electric field energy in the space.

Fig. 8 shows the cross section of an inductor with single-layer N-turn winding. The cross-section of the core is rectangular. a and b are half of the height and width as defined in (26) and (27), respectively. r_l is the average radius of the core as defined in (28). The radius of the winding wire is r_w. The distance between the center of the wire to the surface of the core is d_{tc}. r_{wi} and r_{wo}

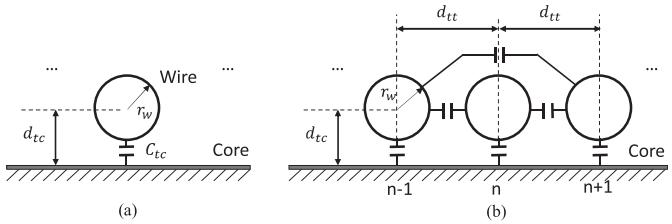

Fig. 9. (a) Single wire over ground. (b) Parallel wires over ground.

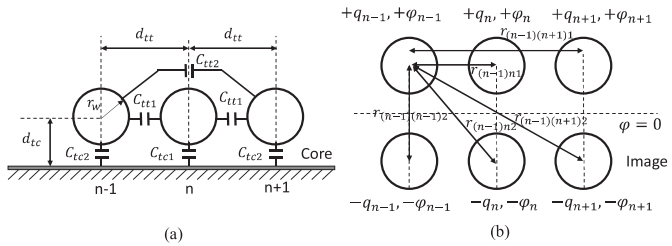

Fig. 10. (a) Parasitic capacitance. (b) Solving capacitance with image theory.

are radii of the winding turns to the center line of the core as defined in (29), (30), and Fig. 8

$$a = \frac{h}{2} \tag{26}$$

$$b = \frac{R_o - R_i}{2} \tag{27}$$

$$r_l = \frac{R_o + R_i}{2} \tag{28}$$

$$r_{wi} = r_l - b - d_{tc} \tag{29}$$

$$r_{wo} = r_l + b + d_{tc}. \tag{30}$$

In most studies in the literature, such as [3], [10], [11], and [15], two assumptions are made. First, if d_{tc} is much smaller than the distance d_{tt} between two adjacent turns, the turn-to-turn capacitance can be ignored, and the turn-to-core capacitance per unit length can be calculated based on a wire-over-ground model [12], as shown in Fig. 9(a), where the magnetic core is an equipotential body due to its high permittivity, so it can be taken as the reference ground. Second, when $d_{tt} << d_{tc}$, one layer winding can be modeled as a copper sheet. The capacitance between the winding layer and the core can be calculated based on parallel plate capacitor theory. However, for many actual inductors, the two assumptions may not hold.

This article will employ the parallel wires-over-ground model in Fig. 9(b). There are parasitic capacitances between any two turns, and between any turn and the core. Since most of the electric field is concentrated in the space between the turn and the core, and between two adjacent turns [3], to simplify the calculation, in Fig. 10(a), when calculating turn-to-core capacitance per unit length C_{tc1} and turn-to-turn capacitance per unit length C_{tt1} for the nth turn, only the parasitic capacitance related to the nth turn, and the adjacent $(n-1)$th and $(n+1)$th turns will be considered. C_{tc2} and C_{tt2} are the turn-to-core and turn-to-turn capacitance per unit length, respectively, for the $(n-1)$th and $(n+1)$th turns. The effect of other winding turns on these parasitic capacitances is ignored in Fig. 10. The image theory can be used in Fig. 10(b) to solve the parasitic capacitance per unit length. The charge per unit length and potentials of the three turns are defined as q_{n-1} and φ_{n-1}, q_n and φ_n, and q_{n+1} and φ_{n+1}, respectively. Their images carry inverse charges and potentials, respectively. The distances between any two turns are defined in Fig. 10(b).

In Fig. 10(b), φ_{n-1} is given by

$$\begin{aligned}\varphi_{n-1} \approx & -\frac{-q_{n-1}}{2\pi\varepsilon_0}\cosh^{-1}\left(\frac{r_{(n-1)(n-1)2}}{2r_w}\right) \\ & -\frac{q_n}{2\pi\varepsilon_0}\ln\left(\frac{r_{(n-1)n1}}{r_w}\right) - \frac{-q_n}{2\pi\varepsilon_0}\ln\left(\frac{r_{(n-1)n2}}{r_w}\right) \\ & -\frac{q_{(n+1)}}{2\pi\varepsilon_0}\ln\left(\frac{r_{(n-1)(n+1)1}}{r_w}\right) \\ & -\frac{-q_{n+1}}{2\pi\varepsilon_0}\ln\left(\frac{r_{(n-1)(n+1)2}}{r_w}\right) \\ = & \frac{q_{n-1}}{2\pi\varepsilon_0}\cosh^{-1}\left(\frac{r_{(n-1)(n-1)2}}{2r_w}\right) + \frac{q_n}{2\pi\varepsilon_0}\ln\left(\frac{r_{(n-1)n2}}{r_{(n-1)n1}}\right) \\ & + \frac{q_{n+1}}{2\pi\varepsilon_0}\ln\left(\frac{r_{(n-1)(n+1)2}}{r_{(n-1)(n+1)1}}\right).\end{aligned} \tag{31}$$

Similarly, φ_n and φ_{n+1} can be solved. To simplify the equations, notations F, F_1, and F_2 are defined as (32)–(34) in the following:

$$F = \cosh^{-1}\left(\frac{r_{(n-1)(n-1)2}}{2r_w}\right) = \cosh^{-1}\left(\frac{d_{tc}}{r_w}\right) \tag{32}$$

$$F_1 = \ln\left(\frac{r_{(n-1)n2}}{r_{(n-1)n1}}\right) = \ln\left(\sqrt{1+\left(\frac{2d_{tc}}{d_{tt}}\right)^2}\right) \tag{33}$$

$$F_2 = \ln\left(\frac{r_{(n-1)(n+1)2}}{r_{(n-1)(n+1)1}}\right) = \ln\left(\sqrt{1+\left(\frac{d_{tc}}{d_{tt}}\right)^2}\right). \tag{34}$$

The voltage potentials can thus be expressed as

$$\begin{pmatrix}\varphi_{n-1}\\ \varphi_n\\ \varphi_{n+1}\end{pmatrix} = \frac{1}{2\pi\varepsilon_0}\begin{pmatrix}F & F_1 & F_2\\ F_1 & F & F_1\\ F_2 & F_1 & F\end{pmatrix}\begin{pmatrix}q_{n-1}\\ q_n\\ q_{n+1}\end{pmatrix}. \tag{35}$$

Therefore, the charges can be solved in

$$\begin{aligned}\begin{pmatrix}q_{n-1}\\ q_n\\ q_{n+1}\end{pmatrix} &= 2\pi\varepsilon_0 \\ &\times \frac{\begin{bmatrix}F^2-F_1^2 & -F_1(F-F_2) & F_1^2-FF_2\\ -F_1(F-F_2) & F^2-F_2^2 & -F_1(F-F_2)\\ F_1^2-FF_2 & -F_1(F-F_2) & F^2-F_1^2\end{bmatrix}}{(F-F_2)(F^2+FF_2-2F_1^2)}\begin{pmatrix}\varphi_{n-1}\\ \varphi_n\\ \varphi_{n+1}\end{pmatrix}.\end{aligned} \tag{36}$$

Based on Fig. 10, the charges can also be represented with capacitance per unit length as

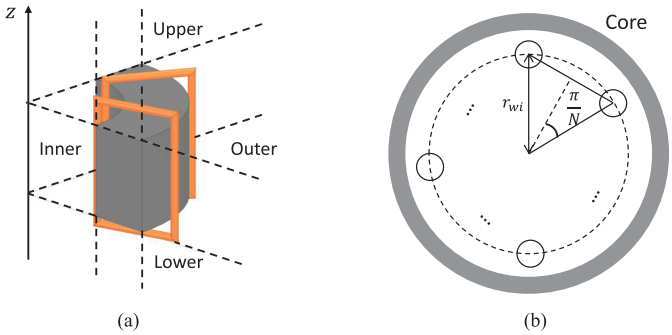

Fig. 11. (a) Regions for electric field energy analysis. (b) Distance between two adjacent turns in the inner region.

Because (36) and (37) shown at the bottom of this page, are equivalent, C_{tc1} can be solved

$$C_{tc1} = 2\pi\varepsilon_0 \frac{F - 2F_1 + F_2}{F^2 - 2F_1^2 + F_2 F} \approx \frac{2\pi\varepsilon_0}{F + 2F_1}. \tag{38}$$

By plugging in F and F_1 to (38), C_{tc1} is

$$C_{tc1} = \frac{2\pi\varepsilon_0}{\cosh^{-1}\left(\frac{d_{tc}}{r_w}\right) + 2\ln\left(\sqrt{1 + \left(\frac{2d_{tc}}{d_{tt}}\right)^2}\right)}. \tag{39}$$

The C_{tt1} in Fig. 10(a) can be solved and simplified similarly

$$C_{tt1} = \frac{2\pi\varepsilon_0 \ln\left(\sqrt{1 + \left(\frac{2d_{tc}}{d_{tt}}\right)^2}\right)}{\left[\cosh^{-1}\left(\frac{d_{tc}}{r_w}\right)\right]^2 - \left[\ln\left(\sqrt{1 + \left(\frac{2d_{tc}}{d_{tt}}\right)^2}\right)\right]^2}. \tag{40}$$

B. Electric Field Energy in the Space

It should be pointed out that, the distance of two adjacent turns is not constant around the turns. The distance of the two adjacent turns on the inner side of the core is smaller than that on the outer side. Also, the distance of two adjacent turns on the top and bottom sides of the core is a function of ρ. To calculate the electric field energy, inner, outer, upper, and lower regions are identified in Fig. 11. The winding length, which is given by (41) and (42) in the following, is l_i, l_o, l_m, and l_m in these regions, respectively:

$$l_i = l_o = 2a \tag{41}$$

$$l_m = \sqrt{(r_{wo} - r_{wi})^2 + 2r_{wo}r_{wi}\left(1 - cos\frac{\pi}{N}\right)}. \tag{42}$$

The distance (d_{tti}) between the two adjacent turns in the inner region is given by (43) as illustrated in Fig. 11(b). The distance (d_{tto}) in outer region is given by (44). The average distance (d_{ttm}) in upper and lower regions is given by (45) in the following:

$$d_{tti} = 2r_{wi}\sin\left(\frac{\pi}{N}\right) \tag{43}$$

$$d_{tto} = 2r_{wo}\sin\left(\frac{\pi}{N}\right) \tag{44}$$

$$d_{ttm} = 2r_{l}\sin\left(\frac{\pi}{N}\right). \tag{45}$$

Ignoring the fringing effect on the two ends of each region, the electric field energy stored in the four regions can be calculated. The calculation for the inner region is taken as an example below. Since the core has high permittivity, it can be regarded as an equal-potential body, and its potential equals the average of the potentials of the inductor's two winding terminals [15]. Also, the voltage distributed along the winding is assumed to be even. Therefore, the electric field energy $E_{tcn,i}$ in the space between the inner part of the nth turn and the core can be expressed as

$$E_{tcn,\,i} = \frac{1}{4}\int_{l_{sn}}^{l_{sn}+l_i} C_{tc1,i}\left(\frac{x}{l_i + l_o + 2l_m}\frac{V_L}{N} - \frac{V_L}{2}\right)^2 dx \tag{46}$$

where V_L/N is the voltage across one turn, $V_L/2$ is the voltage potential of the core, and $l_{sn} = (n-1)(l_i + l_o + 2l_m)$; $C_{tc1,i}$, the turn-to-core capacitance in inner region, can be calculated by replacing d_{tt} in (39) with the d_{tti} in (43).

The total energy $E_{tc,i}$ in the space between turns and the core in inner region is given by

$$E_{tc,i} = \sum_{n=1}^{N} E_{tcn,i} \approx \frac{{V_L}^2}{48} N l_i C_{tc1,i}. \tag{47}$$

The electric field energy in the other three regions can be calculated in a similar way so it will not be repeated here. The total turn-to-core electric field energy E_{tc} can be calculated as

$$E_{tc} = \frac{N{V_L}^2}{48}\left(l_i C_{tc1,i} + l_o C_{tc1,o} + 2l_m C_{tc1,ul}\right) \tag{48}$$

where $C_{tc1,o}$ and $C_{tc1,ul}$ are the turn-to-core capacitances in the outer and upper/lower regions, respectively, and can be calculated based on (39) by replacing d_{tt} with d_{tto} in (44) or d_{ttm} in (45).

Based on (2), EPC$_{tc}$, part of EPC, due to E_{tc} is given by

$$EPC_{tc} = \frac{N}{12}\left(l_i C_{tc1,i} + l_o C_{tc1,o} + 2l_m C_{tc1,ul}\right). \tag{49}$$

The next step is to calculate the electric field energy in the space between adjacent turns. First, $C_{tt1,i}$, the turn-to-turn capacitance per unit length in the inner region can be calculated by replacing d_{tt} in (40) with the d_{tti} in (43). The voltage difference between two adjacent turns is V_L/N, except that between the first and the last turn, which equals $(V_L - V_L/N)$. Therefore,

$$\begin{pmatrix} q_{n-1} \\ q_n \\ q_{n+1} \end{pmatrix} = \begin{pmatrix} C_{tc2} + C_{tt1} + C_{tt2} & -C_{tt1} & -C_{tt2} \\ -C_{tt1} & C_{tc1} + 2C_{tt1} & -C_{tt1} \\ -C_{tt2} & -C_{tt1} & C_{tc2} + C_{tt1} + C_{tt2} \end{pmatrix} \begin{pmatrix} \varphi_{n-1} \\ \varphi_n \\ \varphi_{n+1} \end{pmatrix} \tag{37}$$

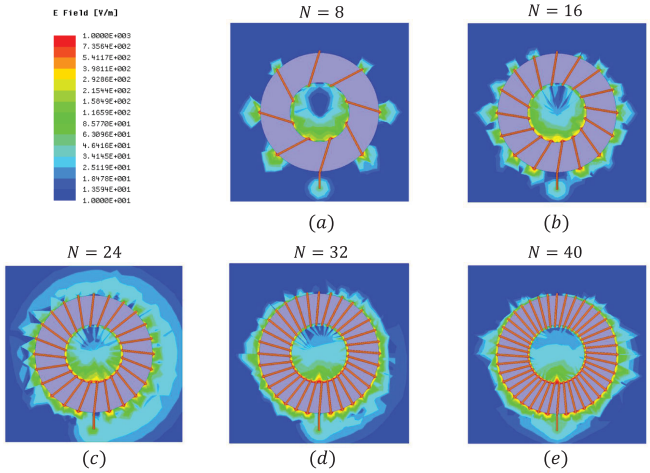

Fig. 12. Simulated electric field in the space with (a) 8 turns, (b) 16 turns, (c) 24 turns, (d) 32 turn, and (e) 40 turns.

the total electric field energy between adjacent turns in the inner region ($E_{tt,i}$) can be calculated as in

$$E_{tt,i} = \frac{C_{tt1,i} l_i}{4} \left[(N-1) \left(\frac{1}{N} V_L \right)^2 + \left(\frac{N-1}{N} V_L \right)^2 \right]. \tag{50}$$

The calculation of electric field energy between adjacent turns for other regions is similar. So, the total electric field energy between the adjacent turns can be expressed as

$$E_{tt} = \frac{C_{tt1,i} l_i + C_{tt1,o} l_o + 2C_{tt1,ul} l_m}{4} \frac{N-1}{N} {V_L}^2 \tag{51}$$

where $C_{tt1,o}$ and $C_{tt1,ul}$ are calculated by replacing d_{tt} in (40) with d_{tto} and d_{ttm} in (44) and (45), respectively.

Based on (2), EPC$_{tt}$, part of EPC, due to E_{tt} is given by

$$EPC_{tt} = \frac{N-1}{N} \left(C_{tt1,i} l_i + C_{tt1,o} l_o + 2C_{tt1,ul} l_m \right). \tag{52}$$

Finally, EPC_{Sp}, part of the EPC, due to the total electric field energy in the space can be calculated from (49) and (52) as follows:

$$EPC_{Sp} = EPC_{tc} + EPC_{tt}. \tag{53}$$

In order to verify the analysis above, simulations were conducted in Ansys HFSS with N varying from 8 to 48. The parameters used in the simulations are: $h = 12.7$ mm, $R_o = 19$ mm, $R_i = 9.5$ mm, $r_l = 14.3$ mm, $a = 6.35$ mm, $b = 4.78$ mm, $d_{tc} = 0.472$ mm, and $r_w = 0.322$ mm. Fig. 12 shows the simulated electric field on the plane of $z = 0$ (center plane) for different number of turns. It is shown that the electric field energy is concentrated in the space between the wire and the core because $d_{tc} << d_{tt}$ and the large surface area of the core. Because of this, it is expected that EPC$_{tc}$ should be dominant. The electric field is also strong in the space between the two winding terminals (the two are overlapped in Fig. 12) but because of the small space, it will not contribute to EPC$_{Sp}$ as much as EPC$_{tc}$.

The simulated EPC$_{Sp}$ due to the electric field energy in the space is compared with the calculated EPC$_{Sp}$ in Fig. 13. The simulation result matches the calculated with less than 5% error.

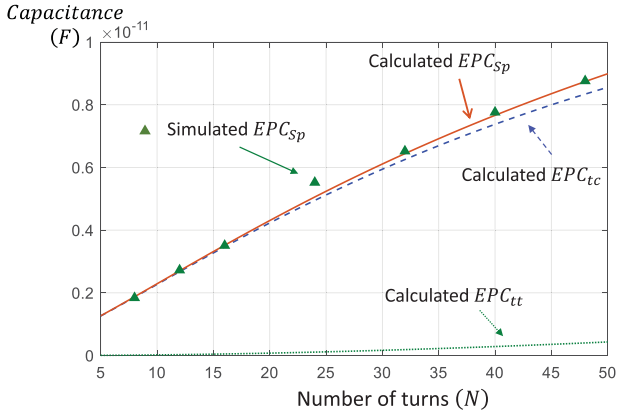

Fig. 13. Comparison of the calculated and simulated EPC$_{Sp}$.

Also, the calculated EPC$_{tc}$ is much higher than EPC$_{tt}$ as shown in Fig. 13, which agrees with the observation in Fig. 12. It is shown that EPC$_{tt}$, EPC$_{tc}$, and EPC$_{Sp}$ increase as N increases. Because of this, if EPC$_{Sp}$ dominates the total EPC, the resonant frequency due to L and EPC$_{sp}$ will not be a constant when N increases.

Based on the above-mentioned results, as N increases, the EPC due to the electric field energy in the space also increases, whereas the EPC due to the electric field energy in the core decreases. Therefore, an optimal N exists in inductor design for the minimum EPC. However, the minimum EPC does not necessarily lead to the highest HF impedance, which will be discussed later.

C. Optimize the Number of Winding Turns

The number of winding turns can be optimized to achieve high HF impedance. Although conclusions and techniques about the electric field energy inside the core in Section II-B–D have been derived from (7)–(22) in Section II-A, directly calculating EPC and EPR is impractical as it is very complicated. Furthermore, important parameters, such as the permittivity of Mn-Zn ferrite, are hardly provided by manufacturers. A practical way to find the optimal number of winding turns is proposed below.

It has been derived in Section II-A that the HF admittance $|Y_L|$ due to the core is inversely proportional to N^2, so in practice, the inductor impedance with one turn winding can be first measured. If the measured EPC and EPR are defined as EPC$_{\text{core1}}$ and EPR$_{\text{core1}}$, the HF impedance $|Z_L| = |I/Y_L|$ of the inductor with N-turn winding at a given frequency f_{op} can be derived as a function of N as

$$|Z_L| = \frac{1}{\sqrt{\left[\omega_{op}\left(EPC_{Sp}(N) + \frac{EPC_{core1}}{N^2}\right)\right]^2 + \left(\frac{1}{N^2 EPR_{core1}}\right)^2}} \tag{54}$$

where $\omega_{op} = 2\pi f_{op}$ and EPC$_{\text{Sp}}$ is given by (53). In order to find the optimal N to have the highest impedance at a certain frequency, the curve of $|Z_L|$ as a function of N at that frequency can be plotted in a graph. Based on the curve, the optimal N with the highest HF impedance can be identified.

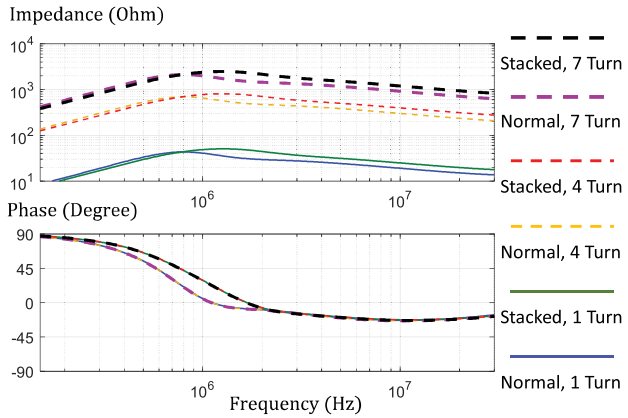

Fig. 14. Measured impedances of normal and stacked inductors with various N.

IV. Experimental Verification

To verify the theory and technique developed in Section II, the measured impedance of an inductor with two toroidal magnetic cores (04J3806TC, J material, $R_O = 19\,\text{mm}$, $R_i = 9.5\,\text{mm}$, $h = 6.35\,\text{mm}$, Magnetic Inc.) stacked in the z-direction is compared with the measured impedance of an inductor with a single toroidal magnetic core (04J3813TC, J material, $R_O = 19\,\text{mm}$, $R_i = 9.5\,\text{mm}$, $h = 12.70\,\text{mm}$, Magnetic Inc.) from 150 kHz to 30 MHz. The winding wire size is AWG#22 ($r_w = 0.322\,\text{mm}$). The stacked cores and the single core have the same width-to-height ratio, MPL, and A_e. The impedances are compared as N is 1, 4, and 7. Since N is small, based on the conclusion in Section III-B, EPC_{Sp} is small, so the electric field energy is mostly concentrated inside the core. This is evidenced by Fig. 14.

First, from Fig. 14, it is obvious that the resonant frequencies of inductors with either stacked cores or normal single core are not influenced by N. This is evidenced by the identical zero crossing frequencies of the measured phases. Second, as N is small, the HF impedances of inductors with either stacked cores or normal single core are proportional to N^2, which agrees with the conclusion derived from the electric field energy inside the core. Third, for the inductors with the stacked cores, the resonant frequency is 1.7 MHz, which is higher than 1.1 MHz of the inductor with the single core. Fourth, the HF impedance of the inductors with the stacked cores is 40% higher than those of the inductors with the single core from 3 to 30 MHz because of higher EPR and smaller EPC. These experimental results verified the theory and the technique of applying stacked cores to increase HF impedance developed in Section II. It is, therefore, concluded that, using more number of winding turns or stacked cores on a Mn-Zn toroidal core inductor with a single-layer winding can increase the inductor's impedance at both low and high frequencies as long as the EPC is dominated by the electric field energy inside the core. This is different from the conventional opinion that increasing the number of winding turns will increase EPC and reduce the inductor's HF impedance.

In the next step, calculations and measurements were made to the single core inductor above to verify that an optimal N can achieve the smallest EPC. In the calculations, $d_{tc} = 0.442\,\text{mm}$.

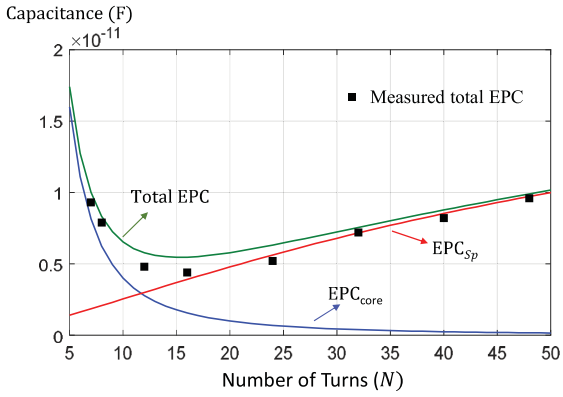

Fig. 15. Comparison of the capacitances due to core and space as N increases.

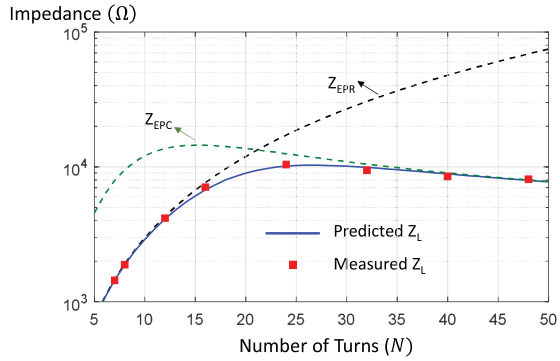

Fig. 16. Calculated and measured impedances at 2 MHz as N varies.

The calculated capacitances as N varies from 5 to 50 are plotted in Fig. 15. It is shown that as N increases, EPC_{core} decreases and EPC_{Sp} increases. As a result, the smallest EPC is at around $N = 15$ when $d\text{EPC}_{\text{core}}/dN = -d\text{EPC}_{Sp}/dN$. Also, in Fig. 15, the measured EPC first decreases and then, increases at around $N = 15$. It matches the calculated total EPC.

Finally, to verify the technique proposed in Section III-C for high HF impedance $|Z_L|$ at desired frequencies, the inductor's impedance is calculated for different N based on (54) at 2 MHz. Fig. 16 shows the comparison of the calculated and measured impedances as N varies. The measured results match the calculated and it is shown that there is an optimal N around 26 for the highest HF impedance. This validates the developed theory and technique.

The N of the smallest EPC and the N of the highest impedance at certain frequencies are usually different. In Fig. 15, EPC_{Sp} is dominant after $N = 15$, so the total EPC increases as N increases, as shown in Fig. 13. In Fig. 16, because Z_{EPR}, the impedance of EPR, is proportional to N^2, as derived in Section II-B, and Z_{EPC}, the impedance of EPC, reduces as N increases if $N>15$, there is a maximum impedance for the paralleled impedance in the inductor model of Fig. 1(b) at around $N = 26$.

V. Parametric Study and Discussions

A. Parametric Study on Sensitive Geometry Parameters

Engineering tolerance exists in inductor manufacturing, so it is necessary to investigate its effect on the proposed HF

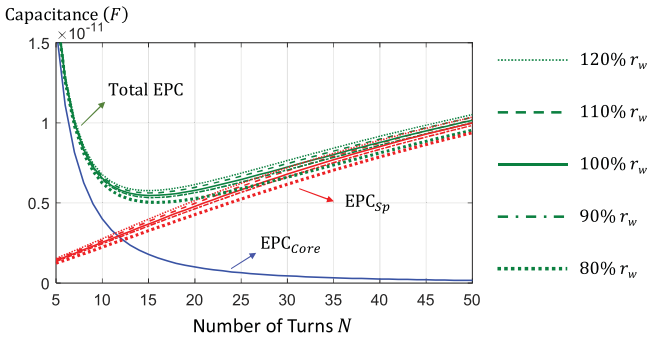

Fig. 17. $\mathrm{EPC_{Sp}}$ and total EPC as the wire radius varies.

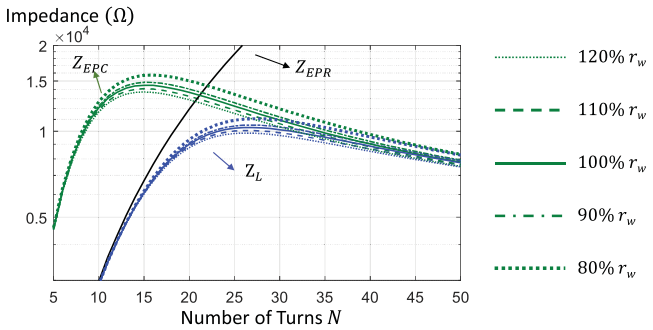

Fig. 18. Impedances of the total EPC and the inductor at 2 MHz as r_w varies.

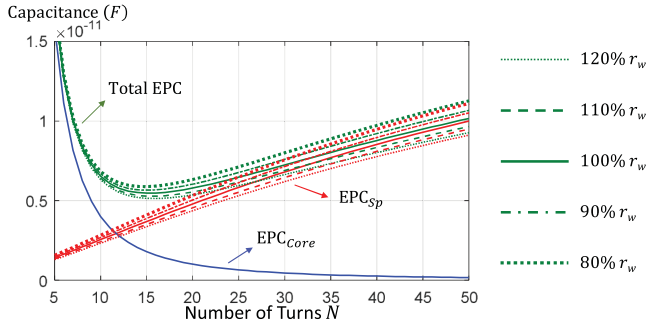

Fig. 19. $\mathrm{EPC_{Sp}}$ and total EPC as d_{tc} varies.

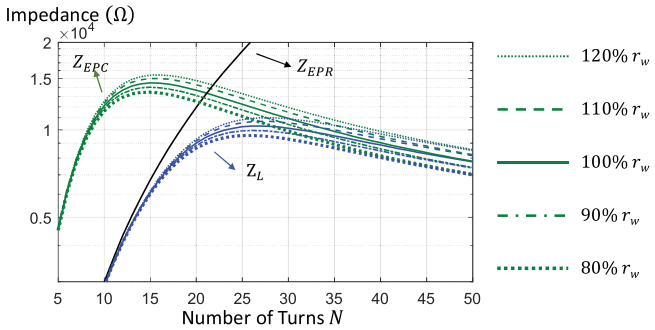

Fig. 20. Impedances of the total EPC and the inductor at 2 MHz as d_{tc} varies.

impedance improving techniques by conducting a parametric study on the sensitive parameters. Based on (39), (40), and Fig. 13, the sensitive parameters are winding wire radius r_w and winding turn-to-core distance d_{tc}. The turn-to-turn distance d_{tt} is not a sensitive parameter because the electric field energy is concentrated in the space between the wire and the core.

Fig. 17 shows the calculated $\mathrm{EPC_{Sp}}$, $\mathrm{EPC_{Core}}$, and total EPC as r_w has a $\pm 20\%$ deviation. $\mathrm{EPC_{Core}}$ is unchanged because it is not influenced by the sensitive parameters based on (13), (14), and (17). From Fig. 17, the variations of $\mathrm{EPC_{Sp}}$ and total EPC are less than $\pm 10\%$, and the number of turns for the minimum total EPC is still very close to 15, so it is not sensitive to r_w.

Fig. 18 shows the impedances of the total EPC and the inductor at 2 MHz as r_w has a $\pm 20\%$ deviation. The impedance variations of the total EPC and the inductor are less than $\pm 10\%$, and the number of turns for the maximum inductor impedance at 2 MHz is still very close to 26, so it is not sensitive to r_w.

Fig. 19 shows the calculated $\mathrm{EPC_{Sp}}$, $\mathrm{EPC_{Core}}$, and total EPC as d_{tc} has a $\pm 20\%$ deviation. Fig. 20 shows the impedances of the total EPC and the inductor at 2 MHz as d_{tc} has a $\pm 20\%$ deviation. A similar conclusion is drawn to that from Figs. 17 and 18. The numbers of turns for the minimum total EPC and the maximum inductor impedances are not sensitive to d_{tc}.

B. Discussions

Mn-Zn ferrite material with high permeability is popularly used in industrial EMI/RFI filters because modern power electronics demands high power density and low cost. Because of this, this article focuses on Mn-Zn ferrite cores. Other cores such as Ni-Zn and powder cores are used in different applications. If these cores have smaller permittivity than Mn-Zn cores, the EPC due to the cores is small so the EPC in the space will dominate. As a result, the stacked core structure will not be as efficient as applied to Mn-Zn cores for EPC reduction.

Stacked core structure can improve HF impedance. However, as more cores are stacked, due to the thickness of core coating layers, air gaps between any two adjacent cores will take more space, which leads to increased height. Also, the cost of the inductors may increase. Therefore, the number of the stacked cores should be determined based on the required HF impedance. When there is a limitation to the inductor profile, the HF impedance should be first evaluated for an inductor with a single core. If it cannot meet the impedance requirement, the number of stacked cores can be increased. After the impedance requirement is met, it is unnecessary to further increase the number of stacked cores. To achieve the best performance and manufacturing convenience, for the stacked cores in z-direction in Fig. 7(b) and (c), the cores should have an identical thickness. For the stacked cores in ρ direction in Fig. 7(d) and (e), because the inner cores have higher magnetic flux density than the outer cores, the optimal widths of the cores can be determined by (55) and (56) to reduce the electric field inside the cores, where w_j, w_k, and w_c are the cross-sectional width of the jth, kth, and cth cores; R_j and R_k are the radii of the jth and kth cores; and n is the number of stacked cores

$$\frac{w_j}{w_k} = \frac{R_j}{R_k} \tag{55}$$

$$R_o - R_i = \sum_{c=1}^{n} w_c. \tag{56}$$

For the applications in a harsh environment, high temperatures may change permeability, permittivity, and conductivity of the cores, however, the conclusions, such as the EPC due to the core is reversely proportional to the square of the number of turns, and the stacked core structure helps to reduce the electric field energy in the cores, are still valid. Therefore, in a harsh environment, the proposed structure can still be applied. It should be noted that when designing the optimal number of turns based on (54), the EPC and EPR due to the cores should be measured in the same environment as actual applications.

It should be pointed out that for the inductors with multilayer windings, the electric field energy in the space between winding layers could be significant, so the theory and techniques in this article should be further adapted for the related analysis.

VI. Conclusion

This article investigated the EPC and EPR of Mn-Zn toroidal inductors with a single layer winding based on electromagnetic theory. Based on the investigation, with a given exciting current, the electric and magnetic field intensities inside the core are proportional to N. Power loss and energy inside the core are proportional to N^2. The resonant frequency between L and $\mathrm{EPC}_{\mathrm{core}}$ is independent of N. The electric field energy inside the core significantly contributes to the total EPC when the number of winding turns is not big. EPC due to the electric field energy inside the core is inversely proportional to N^2 and EPR is proportional to N^2. The cores with a square or round cross-sectional shape have higher EPC and smaller EPR than those with larger or smaller width-to-height ratios. Stacked core structure, therefore, has smaller EPC, bigger EPR, and higher HF impedance than conventional single cores. It is also found that the electric field energy inside the space between the winding turns and the core contributes to most of the EPC due to the electric field energy in the space if $d_{tc}<<d_{tt}$, and the EPC increases as N increases. There is an optimal N for the minimum total EPC. It is concluded that using more number of winding turns or stacked cores on a Mn-Zn toroidal core inductor with a single-layer winding can increase the inductor's impedance at both low and high frequencies, as long as the impedance is dominated by the electric field energy inside the core when N is relatively small. There is an optimal N for the highest impedance at a desired HF frequency. The optimal N can be predicted based on one-turn impedance measurement and the theory developed in this article. Both FEA and experiments were conducted to validate the developed theory and techniques. A parametric study was conducted to prove that the proposed techniques are valid even with engineering tolerance considered.

References

[1] K. V. Namjoshi, J. D. Lavers, and P. P. Biringer, "Eddy-current power loss in toroidal cores with rectangular cross section," *IEEE Trans. Magn.*, vol. 34, no. 3, pp. 636–641, May 1998.

[2] A. Stadler, M. Albach, and A. Bucher, "Calculation of core losses in toroids with rectangular cross section," in *Proc. 12th Int. Power Electron. Motion Control Conf.*, 2006, pp. 828–833.

[3] L. Dalessandro, F. da Silveira Cavalcante, and J. W. Kolar, "Self-capacitance of high-voltage transformers," *IEEE Trans. Power Electron.*, vol. 22, no. 5, pp. 2081–2092, Sep. 2007.

[4] F. da Silveira Cavalcante and J. W. Kolar, "Small-signal model of a 5 kW high-output voltage capacitive-loaded series-parallel resonant DC-DC converter," in *Proc. IEEE 36th Power Electron. Spec. Conf.*, 2005, pp. 1271–1277.

[5] R. Huang, D. Zhang, and K. Tseng, "Determination of dimension-independent magnetic and dielectric properties for Mn–Zn ferrite cores and its EMI applications," *IEEE Trans. Electromagn. Compat.*, vol. 50, no. 3, pp. 597–602, Aug. 2008.

[6] D. Zhang and R. Huang, "Calculation of effective impedance of common-mode choke made of Mn-Zn ferrite," in *Proc. 17th Int. Zurich Symp. Electromagn. Compat.*, 2006, pp. 391–394.

[7] H. Zhao, Y. Li, Q. Lin, and S. Wang, "The parasitic capacitance of magnetic components with ferrite cores due to time-varying electromagnetic (EM) field," in *Proc. IEEE Energy Convers. Congr. Expo.*, 2018, pp. 3534–3541.

[8] C. Cuellar, W. Tan, X. Margueron, A. Benabou, and N. Idir, "Measurement method of the complex magnetic permeability of ferrites in high frequency," in *Proc. IEEE Int. Instrum. Meas. Technol. Conf.*, 2012, pp. 63–68.

[9] C. A. Balanis, *Antenna Theory: Analysis and Design*, 3rd ed. Hoboken, NJ, USA: Wiley, 2005.

[10] M. Kovacic, Z. Hanic, S. Stipetic, S. Krishnamurthy, and D. Zarko, "Analytical wideband model of a common-mode choke," *IEEE Trans. Power Electron.*, vol. 27, no. 7, pp. 3173–3185, Jul. 2012.

[11] J. Yao, Y. Li, H. Zhao, and S. Wang, "Design of CM inductor based on core loss for radiated EMI reduction in power converters," in *Proc. IEEE Appl. Power Electron. Conf. Expo.*, Anaheim, CA, USA, 2019, pp. 2673–2680.

[12] C. R. Paul, *Analysis of Multiconductor Transmission Lines*, 2nd ed. Hoboken, NJ, USA: Wiley, 2007.

[13] S. Wang, F. C. Lee, and W. G. Odendaal, "Single layer iron powder core inductor model and its effect on boost PFC EMI noise," in *Proc. IEEE 34th Annu. Conf. Power Electron. Spec.*, Acapulco, Mexico, 2003, pp. 847–852.

[14] Y. Chu, S. Wang, N. Zhang, and D. Fu, "A common mode inductor with external magnetic field immunity, low-magnetic field emission, and high-differential mode inductance," *IEEE Trans. Power Electron.*, vol. 30, no. 12, pp. 6684–6694, Dec. 2015.

[15] B. Liu, R. Ren, F. Wang, D. Costinett, and Z. Zhang, "Winding scheme with fractional layer for differential-mode toroidal inductor," *IEEE Trans. Ind. Electron.*, vol. 67, no. 2, pp. 1592–1604, Feb. 2020.

[16] S. Yamada, E. Otsuki, and T. Otsuka, "AC resistivity of Mn-Zn ferrites," in *Proc. 13th Int. Telecommun. Energy Conf.*, Kyoto, Japan, 1991, pp. 703–708.

[17] F. C. Lee, M. Xu, S. Wang, and B. Lu, "Design challenges for distributed power systems," in *Proc. CES/IEEE 5th Int. Power Electron. Motion Control Conf.*, 2006, pp. 1–15.

Yiming Li (Student Member, IEEE) received the B.Sc. degree from Zhejiang University, Zhejiang, China, in 2015, and the Ph.D. degree from the University of Florida, Gainesville, FL, USA, in 2019, both in electrical engineering.

He has authored and coauthored more than 18 IEEE journal and conference papers since 2017. He works on transformer and electromagnetic interference filter design and optimization for switching mode power supplies. His research interests include electromagnetic interference and compatibility in power electronic systems.

Shuo Wang (Fellow, IEEE) received the Ph.D. degree in electrical engineering from Virginia Tech, Blacksburg, VA, USA, in 2005.

He is currently a Full Professor with the Department of Electrical and Computer Engineering, University of Florida, Gainesville, FL, USA. He has authored and coauthored more than 200 IEEE journal and conference papers and holds around 30 pending/issued U.S./international patents.

Dr. Wang was the recipient of the Best Transaction Paper Award from the IEEE Power Electronics Society in 2006, two William M. Portnoy Awards for the papers published in the IEEE Industry Applications Society in 2004 and 2012, and the prestigious National Science Foundation CAREER Award in 2012. He is an Associate Editor for the IEEE Transactions on Industry Applications and IEEE Transactions on Electromagnetic Compatibility. He was a Technical Program Co-Chair for the IEEE 2014 International Electric Vehicle Conference.